Hydraulic fracturing in laminated reservoirs

E. Siebrits
Schlumberger, SPC/EAD, Houston

A.P. Peirce
Dept. of Mathematics, University of British Columbia, Vancouver

Presented at the Workshop on Three Dimensional and Advanced Hydraulic Fracture Modeling, held in conjunction with the Fourth North American Rock Mechanics Symposium, July 29, 2000, Seattle

ABSTRACT: We present a method for the efficient and accurate modeling of planar three-dimensional (3D) hydraulic fracture growth in laminated reservoirs. We verify the scheme against available numerical and analytical results. We also demonstrate the effect of layering on both the shape and extent of a planar fracture that crosses a number of elastic layers.

1 INTRODUCTION

Since the 1960s, there have been many theoretical and experimental investigations into the effects of elastic layering on the growth of hydraulic fractures (e.g., [1-15]). Numerical models have been developed to model the effects of layering, but most have been at best partially successful in this respect (e.g., [24, 25, 26]). Such schemes are prone to significant numerical errors under certain conditions, such as when thin layers (relative to the fracture dimensions) are present in the model. The main issue at stake is the complexity in deriving a complete mathematical and numerical description of the effects of layers.

In this paper, we describe an algorithm to numerically couple the elasticity and fluid flow relations that describe the growth of a hydraulic fracture in a laminated reservoir. The elastic model used to describe the layering is highly accurate and efficient. We show the results of three verification problems to test the accuracy of the model. Finally, we show an example that demonstrates the effect that changes in elastic properties have on both the fracture width and extent of hydraulic fracture growth.

2 MODEL DESCRIPTION

We make the following assumptions. The reservoir host rock is linear elastic. All layers are assumed to be parallel to each other, as depicted schematically in Fig. 1. Each layer is defined by a unique Young's modulus and Poisson's ratio. Each layer may, in general, be associated with unique lateral confining stress, rock toughness, and leakoff properties. All interfaces between successive layers are assumed to be fully bonded. No interfacial slip or delamination is allowed between layers. Layer thicknesses can be varied from 0.2 m to over 250 m. A single plane, assumed to lie orthogonal to the layer interfaces, contains the hydraulic fracture. The hydraulic fracture is forced to remain planar during growth, and can intersect any number of layers.

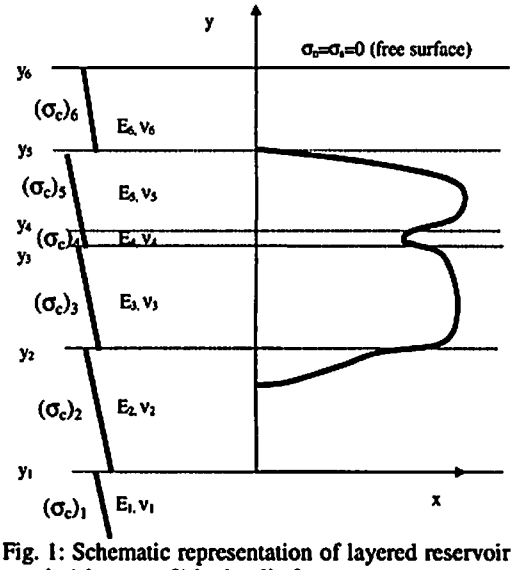

Fig. 1: Schematic representation of layered reservoir and symmetric (about $x = 0$) hydraulic fracture

3 GOVERNING EQUATIONS

There are essentially three unknowns in the hydraulic fracturing problem – fracture width, fluid pressure, and fracture front location. This combination

of unknowns assumes that we have imposed a time step on the system. We can thus iterate on the fracture front at marker points along the perimeter, using tip velocity data, until convergence is achieved.

An alternative approach, that we have adopted, is to iterate on the time step. This combination assumes that we have a predefined fracture front at the start of the current time step, obtained by incremental growth from data at the end of the previous time step. This approach is also computationally less intensive than the former.

In either case, we require three sets of equations to solve the problem. These equations are the elasticity and fluid flow equations, and an integral equation equating the volume of injected fluid with the volume of fluid stored in the fracture plus the volume that has leaked off into the reservoir.

We use a 3D displacement discontinuity method [19] to describe the elastic response of the layered rock mass to the growing fluid-filled hydraulic fracture. Because we currently impose the restriction that the fracture plane is orthogonal to the layering, we require no shear terms in the equations. A full derivation of the equations is given in [16-17], and will not be repeated here. We can write the final set of algebraic equations as

$$Cw = p - \sigma_c \tag{1}$$

where

w = fracture width
p = fluid pressure
σ_c = confining stress
C = influence coefficient matrix

and the elastic influence matrix, C, is a function of the fracture geometry, the elastic properties of each layer, and the layer thicknesses.

The fluid flow process in the fracture is assumed to behave Poiseuille-like, and is described by the following two-dimensional (2D) continuity equation (for Newtonian fluids):

$$\frac{\partial w}{\partial t} + div(q) = v_s - 2v_L \tag{2}$$

where

$$q = wv \tag{3}$$

$$v = (v_x, v_y)$$

$$v_x = -\frac{w^2}{12\mu}\frac{dp}{dx} \tag{4a}$$

$$v_y = -\frac{w^2}{12\mu}\frac{dp}{dy} \tag{4b}$$

$$v_L = v_L(x,y,t) = \frac{C_L}{\sqrt{t - t_{beg}(x,y)}} \tag{5}$$

$$v_s = v_s(x,y,t) = Q(x,y,t)\delta(x,y) \tag{6}$$

and

v_L = Carter leak-off velocity
v_s = source velocity
t = current time
t_{beg} = time at which current point started leak-off
C_L = Carter leakoff coefficient
Q = current injection rate
μ = fluid viscosity

In the aforegoing, no mention has been made of the material toughness of each layer. In our current formulation, we assume zero toughness in each layer.

4 DISCRETIZED EQUATIONS

As noted in Section 3, we employ a displacement discontinuity method to describe the elastic response of the laminated reservoir due to the injected fluid-filled hydraulic fracture. The fluid flow equations are discretized using a finite difference scheme. In this section, we first describe the meshing strategy before elaborating on some details of the discretization of the elasticity and fluid flow equations.

4.1 *Meshing strategy*

The meshing strategy is important, as it dictates the entire development of the numerical model. There are two basic options. The first option is to use triangular elements (e.g., Delaunay triangulation). This allows us to match the fracture front with the numerical mesh in a natural manner. However, triangulation requires periodic re-meshing after a number of growth steps. In the case of multiple materials, the cost of regenerating the elastic influence coefficient matrix is expensive. In addition, re-meshing is prone to interpolation errors.

The other option, which we have selected, is to use a regular mesh of rectangular elements. This has the advantage of allowing us to calculate all influ-

ence coefficients once at the start of the simulation. At each growth step, we simply extract the relevant influences required for all active elements. In addition, no coefficient regeneration is required should we, for example, wish to perform another simulation with different layer toughness, confining stresses, leakoff, or injection schedule.

We employ a Fourier-based boundary integral approach to solve the elasticity equations, designed in such a way that we never need to discretize the layer interfaces. This significantly reduces the problem size, and allows us to obtain very accurate fracture widths in a layered material using a very efficient algorithm.

However, a regular mesh poses a unique set of problems at the fracture front. To avoid a binary-like fracture front, we require sophisticated numerical procedures to account for fracture tip elements that are "partially fractured," as will be explained later.

We choose to discretize the fracture plane into a parent mesh of rectangular elements, as shown in Fig. 2. Layer interfaces will not, in general, match up exactly with element edges. We thus allow element subdivision so as to enforce an exact match with layer interfaces (Fig. 3). In the case of a close shave with an interface (e.g., sub-divided element less than ¼ of parent element size), we slightly adjust the interface elevation to match the element edge exactly. Element sub-division is necessary in order to retain fracture width accuracy in the presence of interfaces. Width errors due to mismatched interface positions can be surprisingly large (> 15 %) if sub-division is not used, because the elastic layers influence each other locally. An alternative approach would be to introduce an "averaged" elastic modulus into each element cut by an interface; however it is the authors' experience that this can result in unacceptably large errors in fracture width.

The rectangular parent mesh is binary in nature. However, the fracture front is assumed to be piecewise linear, and can intersect a tip element in a non-binary manner, as shown in Fig. 3. We employ special "edge-correction" adjustments to the elasticity influence coefficient matrix [21] to account for these situations. This allows us to obtain an accurate width result near the fracture tip even though we are employing a binary mesh system. This is demonstrated later in some test problems. The fluid flow equations also take into account the fracture front locations (see Section 4.3).

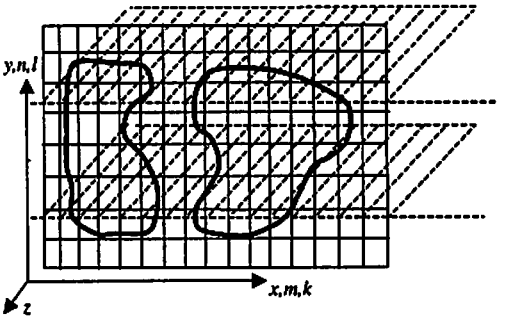

Fig. 2: Schematic representation of vertical oriented parent mesh (solid lines) containing two fractures, and two horizontal interfaces (dashed lines)

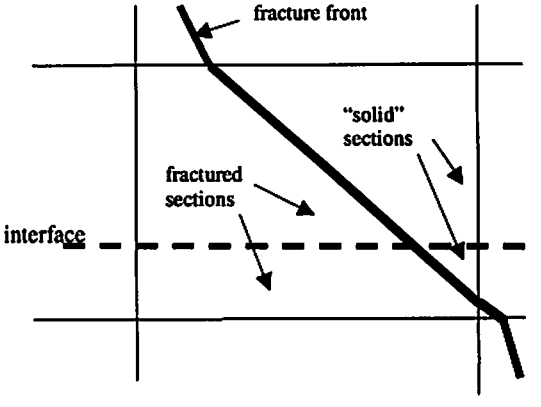

Fig. 3: Partially fractured tip element

4.2 *Elasticity*

The final set of algebraic equations (1) for elasticity can be written as:

$$\sum_{j=1}^{N} C_{ij} w_j = p_i - (\sigma_c)_i, \quad i = 1, N \tag{7}$$

where we have assumed that there are N active elements on the fracture surface at the current time step. In (7), we have assumed a constant variation of displacement discontinuity over each rectangular element, with collocation performed at the center of each element [19].

The influence matrix C contains a complete description of the layered elastic rock mass, including a free surface (if desired). The derivation of C for a layered elastic medium is summarized in [16-17]. Generation of the complete multi-layered elastic influence coefficient matrix for a parent mesh of 64 by

64 elements typically takes less than 1 minute of CPU time on a 450 MHz PC machine.

4.3 *Fluid flow*

The 2D fluid flow in the planar fracture is modeled using a finite difference scheme. Discretization of (2) leads to the following standard system of equations

$$-\sum_{j=1}^{N} A_{ij}(w)p_j = r_i(w), \quad i=1,N \tag{8}$$

where

$$r(w) = v_s - 2v_L - \frac{w_t - w_{t-\Delta t}}{\Delta t} \tag{9}$$

Matrix product $A(w)p$ can be written in terms of contributions from a west, east, south, north, and center node for each finite difference molecule as

$$-A(w)p = a_W p_W + a_E p_E + a_S p_S + a_N p_N + a_C p_C \tag{10}$$

where, for all interior finite difference molecules,

$$a_W = \left.\frac{-w^3}{12\mu(\Delta x)^2}\right|_w$$

$$a_E = \left.\frac{-w^3}{12\mu(\Delta x)^2}\right|_e$$

$$a_S = \left.\frac{-w^3}{12\mu(\Delta y)^2}\right|_s$$

$$a_N = \left.\frac{-w^3}{12\mu(\Delta y)^2}\right|_n \tag{11}$$

$$a_C = -(a_W + a_E + a_S + a_N) \tag{12}$$

The notation used above differentiates between element centers (upper case S, etc.) for the pressure collocation positions in (10) versus element edges (lower case *s*, etc.) for the effective permeability coefficients in (11).

As mentioned earlier, the finite difference stiffnesses (11, 12) can be adjusted at each fracture tip element so as to track the actual fracture front. This is accomplished by adjusting the west, east, south, and/or north arm lengths of each tip molecule to exactly match the local fracture front [27]. This ensures that the finite difference result retains second order accuracy.

5 BOUNDARY CONDITIONS FOR COUPLED PROBLEM

The boundary conditions at the fracture front are important to define, as they completely control the shape of the fracture and the fracture pressure behavior. The boundary condition for the fluid equation in the coupled problem is that the flux is zero at the tip (in the absence of fluid lag [28]):

$$q|_{tip} = 0 \tag{13}$$

The flux boundary condition, because it involves pressure gradients, implies a non-unique solution. However, global mass balance ensures that we can find a unique set of fluid pressures to satisfy all sets of equations.

The flux boundary condition is very difficult to implement on a 2D finite difference mesh containing molecules with adjustable arm lengths along the fracture perimeter [27]. Therefore, we have chosen to implement a (much simpler) fluid pressure boundary condition at the fracture tip. Even though this is a rather artificial choice of boundary condition, we nevertheless obtain accurate results (see Section 8). We are currently in the process of implementing the more rigorous flux boundary condition into the simulator.

6 FRACTURE GROWTH CONTROL

The fracture front advance from one time step to the next is controlled by the magnitude of fluid velocity near the fracture tip. The growth increment of any point along the fracture front is simply the product of the local normal component of fluid velocity and the current time step.

We use a marker method to track the fracture front explicitly, as depicted schematically in Fig. 4. The dashed arrows are the growth vectors from the previous growth step. The arrowheads are then joined together by straight dashed lines. The locations where the dashed lines cut element edges are termed cut points. All cut points are then joined together to form new fracture front segments. The new growth vectors, indicated by the solid arrows, are then assumed to originate from the center of each front segment (one per element). The logic will only allow one growth vector per element, one growth

segment per element, and two cut points per element. Notice that this type of growth logic introduces a natural smoothing of the fracture front because of the combination of dashed pseudo and solid actual fronts that are generated as part of the process.

Whenever the fracture front is concave, multiple growth vectors may enter a new element. If this situation occurs, we delete all but one of the multiple growth vectors. Whenever the fracture front is convex, or if large growth increments are allowed, we can generate situations where potential new tip elements do not contain growth vectors. In these cases, extra front segments are added as needed so that each tip element will contain a front segment, so that the front is unbroken.

Whenever high curvature exists along the front, situations may arise where only one side of a potential tip element is cut by the dashed lines. These situations are not allowed to occur, and the associated growth vectors are deleted. The neighbors of each deleted growth vector are joined up instead to form a smoother front. Deletion of these peninsula-type situations does not cause any artificial control on the front. The front will automatically adjust during the next growth increment according to the fracture growth calculations.

At all times, connectivity must be maintained along the front. All front segment nodes are made aware of their neighbors via a connectivity array. The algorithm performs internal checks to ensure that connectivity is always maintained. This type of front control is quite general. It is possible to grow any number of separate multiple fronts. In addition, there is logic that allows different parts of the same front or separate fronts to merge once they intersect each other. The key to controlling such a system is local autonomy. Each front segment only cares about its neighbor on each side, and is also aware of any potential clash with another incoming front.

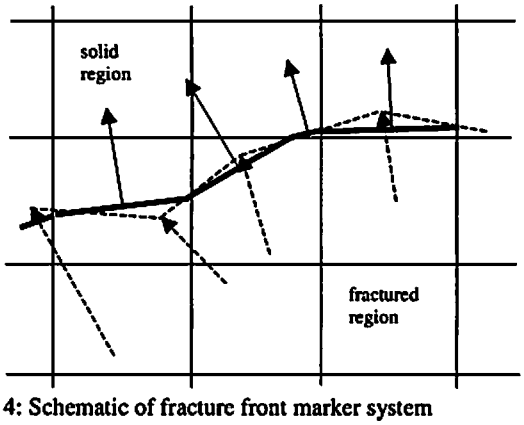

Fig. 4: Schematic of fracture front marker system

In order to demonstrate the complexity allowed by the front-tracking algorithm, we show a composite of a number of growth steps in Fig. 5 for an initial planar three-fracture system that merges into a single pseudo-radial fracture after a number of growth steps. In this simulation, we have assumed that the elastic fractures are driven by the same prescribed constant pressure in each element (i.e., no fluid behavior has been added to the system), under zero toughness and zero confinement conditions. The input parameters used were E = 10 GPa, ν = 0.1, and applied pressure p = 10 MPa. The example demonstrates the ability of the front-tracking algorithm to cope with merging fronts, disappearing islands, and concave sections. The total CPU time for this problem was 7.2 min. on a 450 MHz PC machine, and based on a 100 by 100 parent mesh.

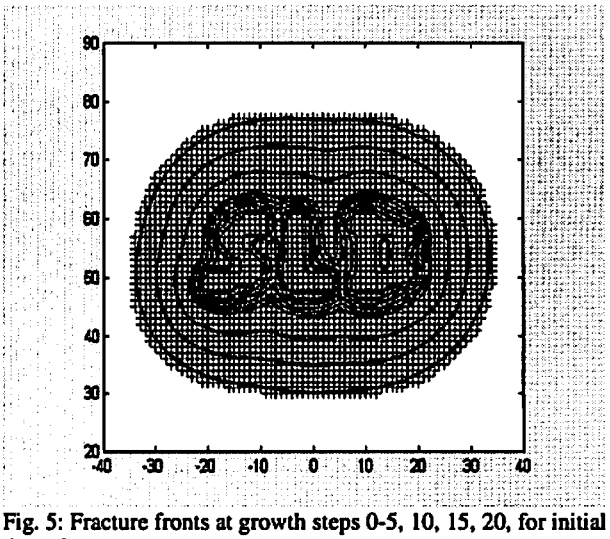

Fig. 5: Fracture fronts at growth steps 0-5, 10, 15, 20, for initial three-fracture system.

7 ELASTICITY-FLUID COUPLING

The elasticity and fluid flow equations are coupled together numerically in an iterative algorithm. In our scheme, there are three sets of unknowns to solve for, viz., the fracture width and fluid pressure on each element, and the time step. There are many ways to couple the elasticity and fluid flow equations together. We present two approaches here.

7.1 *Picard Coupling*

The simplest coupling approach is to use a Picard iterative strategy on width and pressure, with an updated time step calculated at each global iteration based on preservation of volume balance. Picard iteration can be unreliable, however, and is very sensitive to a narrow range of under-relaxation parameters of $0.2 < \alpha < 0.3$ typically. Iteration counts can also be high (10 to 100) depending on the problem being solved and the choice of conversion tolerances, although each iteration is quick. In addition, later iterations are faster than earlier ones given an

efficient iterative solver for the elasticity and fluid flow equation systems. Picard coupling can be summarized as follows:

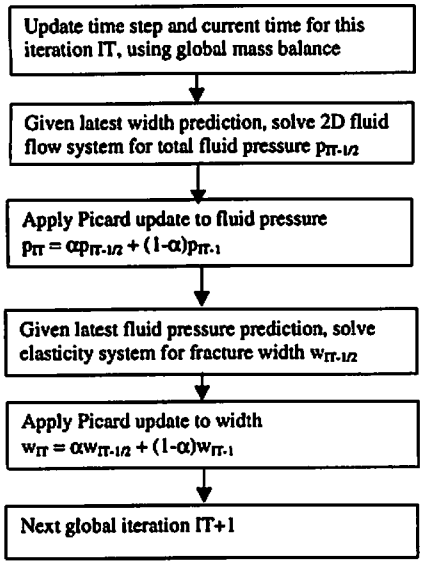

7.2 *Damped Quasi-Newton Coupling*

We favor a damped quasi-Newton scheme, where we simultaneously iterate on width, pressure, and the time step. Iteration counts of 6 to 10 global iterations are typically achieved. Damping is used to ensure that initial guesses do not stray too far from the desired solution, so as to avoid divergence of the solution. This damping procedure is complicated, and will not be described here.

We will present the Newton derivation in one-dimensional (1D) form, for simplicity. The relevant planar 3D equations are given in Appendix B. We will also assume zero leakoff and constant injection rate for simplicity. Recall the elasticity (1), fluid flow (2), and global volume balance equations (the latter follows directly from (2) by integration), which we can write as

$$Cw = p - \sigma_c \tag{14}$$

$$\frac{w_t - w_{t-\Delta t}}{\Delta t} = \left(D(w_t)p'\right)' + K \tag{15}$$

$$V^T w_t = (t_{old} + \Delta t)Q \tag{16}$$

where $(\bullet)' = d(\bullet)/dx$, K is the injection source (or sink) term, $t_{old} = t - \Delta t$, t is the current time, V^T is a vector of integration weights defined by the fractured areas of each element, and superscript T is the transpose. Note that, at all times, we maintain exact volume balance by the use of (16).

Let $(\bar{w}, \bar{p}, \Delta\bar{t})$ be the final (converged) state, and let $(w, p, \Delta t)$ be the initial state at the first iteration. Thus we have

$$(\bar{w} = w + \delta w, \bar{p} = p + \delta p, \Delta\bar{t} = \Delta t + \delta t). \tag{17}$$

Linearization of (14-16) at the final state, after manipulation, gives the following 3 by 3 block system of Newton residual equations:

$$\begin{bmatrix} -C & I & 0 \\ -\dfrac{I}{\Delta t} + B & A & \dfrac{w_t - w_{t-\Delta t}}{(\Delta t)^2} \\ -V^T & 0 & Q \end{bmatrix} \begin{bmatrix} \delta w \\ \delta p \\ \delta t \end{bmatrix} = - \begin{bmatrix} r_w = p - \sigma_c - Cw \\ r_p = Ap + K - \dfrac{w_t - w_{t-\Delta t}}{\Delta t} \\ r_t = -V^T w + (t_{old} + \Delta t)Q \end{bmatrix} \tag{18}$$

where I is the identity matrix, and

$$A = \frac{d}{dx}\left(D(w)\frac{d(\bullet)}{dx}\right) \tag{19}$$

$$B = \frac{d}{dx}\left(D'(w)p'(\bullet)\right) \tag{20}$$

and

$$D'(w) = \frac{dD(w)}{dw} = \frac{w^2}{4\mu} \tag{21}$$

and $(\bullet)$ indicates that A and B operate on δp and δw, respectively. The discretized forms of (19) and (20) are summarized in Appendix A.

The above 3 by 3 block system (18) can be collapsed into a 2 by 2 block system by eliminating the time step equation from the system to obtain

$$\begin{bmatrix} -C & I \\ -\dfrac{I}{\Delta t} + B + \dfrac{\Delta w V^T}{Q(\Delta t)^2} & A \end{bmatrix} \begin{bmatrix} \delta w \\ \delta p \end{bmatrix} = - \begin{bmatrix} r_w \\ r_p - \left(\dfrac{r_t}{Q(\Delta t)^2}\right)\Delta w \end{bmatrix} \tag{22}$$

where $\Delta w = (w_t - w_{t-\Delta t})$. After solution of the 2 by 2 system (22), we can extract the time correction from

$$\delta t = (V^T \delta w - r_t)/Q \qquad (23)$$

The 2 by 2 block form (22) with supplemental calculation (23) is identical to, but better conditioned than, the 3 by 3 block system (18). At first glance, it appears that the 2 by 2 system is less efficient than the 3 by 3 system in terms of storage because the dyadic product $\Delta w V^T$ fills the lower left block of the Jacobian (in the 3 by 3 system the corresponding Jacobian block is sparse and penta-diagonal). However, we can avoid this increased storage by first performing the operation $\Delta w(V^T \delta w)$. The bracketed operation is a dot product. The remaining task is a scalar multiplication. The implication is that the lower left matrix block can be reduced to a sparse penta-diagonal form, with significant storage savings.

7.3 *Start-up solution for coupled algorithm*

The coupled algorithm requires a start-up solution in order to iterate successfully. We use the following scheme. For a point source, we employ a starter fracture of 5 by 5 elements. Initial guesses for fracture width and pressure are obtained by invoking the exact radial solution [20]. Thereafter, at all later time steps, we simply use the maximum fluid pressure from the previous time step as the starting guess on all elements, and find an initial width profile that matches this assumption. In the case of a line source (such as will occur along a perforated wellbore), we employ a corrected version of the exact solution for a KGD-type fracture [23] instead of the exact radial one.

8 TEST PROBLEMS

8.1 *Static partially loaded radial fracture in homogeneous material*

Sneddon [22] provides an exact solution of fracture width as a function of radius for the case of a partially loaded penny crack in a homogeneous material. The exact width, w, is given by

$$w(r) = \frac{8(1-\nu^2)p}{\pi E}\sqrt{c^2 - r^2}\left(1 - \sqrt{1 - a^2/c^2}\right) \qquad (24)$$

where

p = applied fracture pressure over radius $r < a$
c = fracture radius
r = current radius

In our test problem, we choose the centrally loaded region to be defined by $a = c/2$. We used a parent mesh of 24 by 24 square elements to describe the entire fracture. Fig. 6 shows the exact and numerical ('C3D') results. The match is excellent, even close to the fracture tip. This problem demonstrates that our numerical scheme provides highly accurate fracture width results even though we are modeling a curved fracture shape using a coarse binary parent mesh.

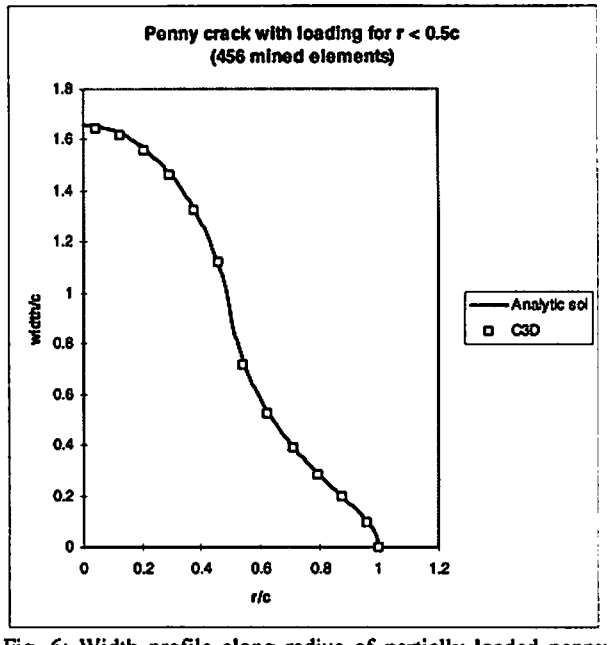

Fig. 6: Width profile along radius of partially loaded penny fracture

8.2 *Static radial fracture in three-layer material*

Lin and Keer [18] have published a set of results for a static radial fracture spanning three elastic layers, as shown in Fig. 7. The Young's modulus of the middle layer is assumed to be E, and the bounding layers have Young's moduli of ηE, where $\eta = 2$, 4, or 10. Fig. 8 shows the normalized fracture width as a function of distance along the y axis for both the Lin and Keer results and our's ('MLAYER3D'). The match is excellent, and demonstrates the ability of our numerical scheme to deal with abrupt changes in layer elastic properties.

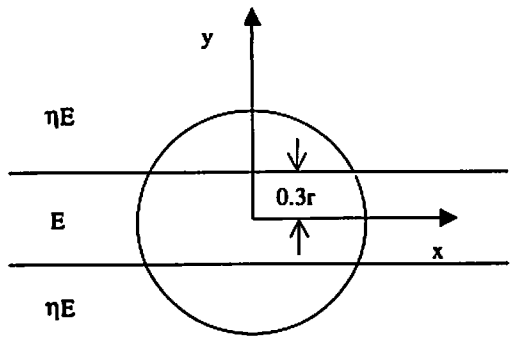

Fig. 7: Geometry of penny fracture spanning three elastic layers.

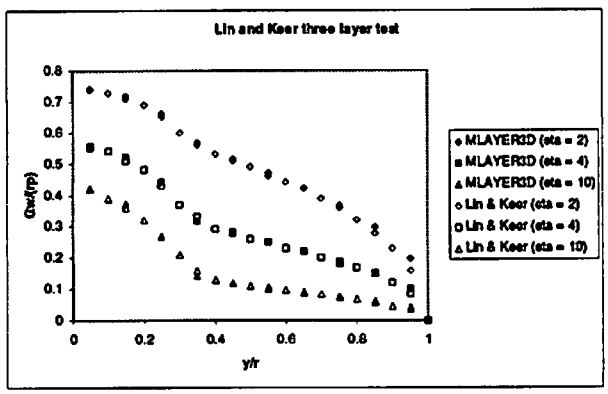

Fig. 8: Normalized width vs. radial distance for three-layer case

8.3 *Fully coupled radial fracture in homogeneous material*

An exact solution for a fluid-driven radial fracture propagating in a homogeneous elastic material is available [20]. The input properties used were $E = 5$ GPa, $\nu = 0.2$, $\Delta x = \Delta y = 5$ m, $Q = 2.5\text{x}10^{-2}$ m^3/s, and $\mu = 0.2$ Pa.s. Fig. 9 shows the fracture width as a function of fracture radius at the 19th growth step (when $t = 92$ min.) for the exact ('UMN') and numerical ('C3D') cases. Fig. 10 shows the fluid net pressure versus radius. Fig. 11 shows the average fracture tip growth rate as a function of current fracture tip radius compared with the exact solution. In all cases, the match is very good, especially considering that no special attention has been given to the asymptotic behavior [20] near the fracture tip. The total CPU time was 9.4 min on a 450 MHz PC machine, and based on a 64 by 64 parent mesh.

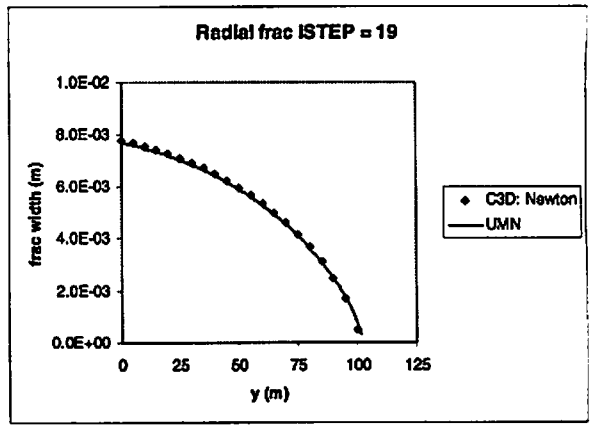

Fig. 9: Width vs. radius at 19th time step

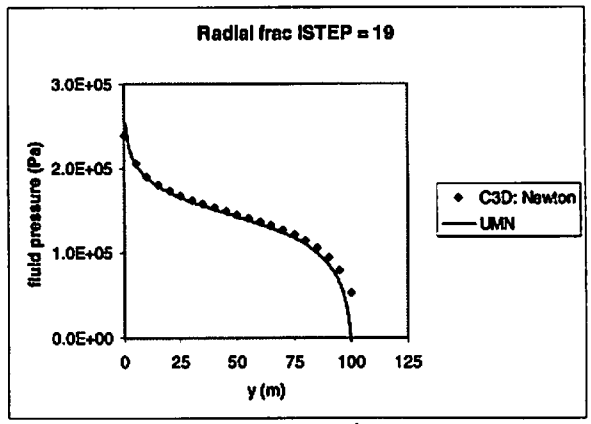

Fig. 10: Net pressure vs. radius at 19th time step

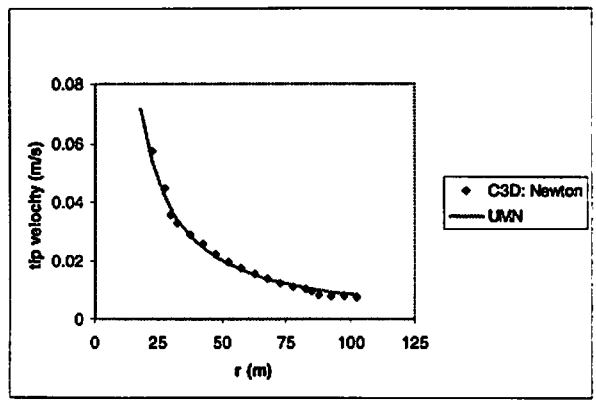

Fig. 11: Average fracture tip velocity vs. fracture tip radius

9 FULLY COUPLED FRACTURE GROWTH IN A MULTI-LAYERED MATERIAL

Table 1 defines the layer properties and thicknesses of a multi-layered reservoir. We grow a hydraulic fracture, starting at the source location shown in Fig 12, under a constant injection rate of $Q = 0.01$ m^3/s. Fluid viscosity is taken to be 1 Pa.s, and the element size is fixed at $\Delta x = \Delta y = 1$ m. The confining stresses

and rock toughness in each layer are assumed to be zero in this hypothetical example.

Layer Thickness (m)	Layer top elevation y (m)	E (GPa)	ν
600	640	66	0.25
10	40	2.2 (= E)	0.25
10	30	22	0.25
20	20	4.4	0.25
1,000	0	4.4	0.25

Table 1: Layer properties for multi-layer problem

Fig. 12 shows the fracture surface at the 28th time step (when t = 7.1 min.). The fracture clearly favors growth into the material with lowest Young's modulus. The upper barrier zone with high Young's modulus prevents uncontrolled height growth. Fig. 13 shows an oblique view of the fracture half-width over the fracture surface, and we can see how the layering dramatically affects the fracture width profile.

It is important to note that no confining stress was included in this simulation - all width changes across interfaces are purely a function of changes in elastic properties. The use of a pseudo 3D model (that uses a single averaged Young's modulus and Poisson's ratio for all layers) would result in a radial fracture shape with elliptical width profile. We see that a correct description of the elastic properties of the layered reservoir has a significant influence on both the fracture width and fracture extent. The total CPU time for this problem was 31 min. on a 450 MHz PC machine, using a 64 by 64 parent mesh.

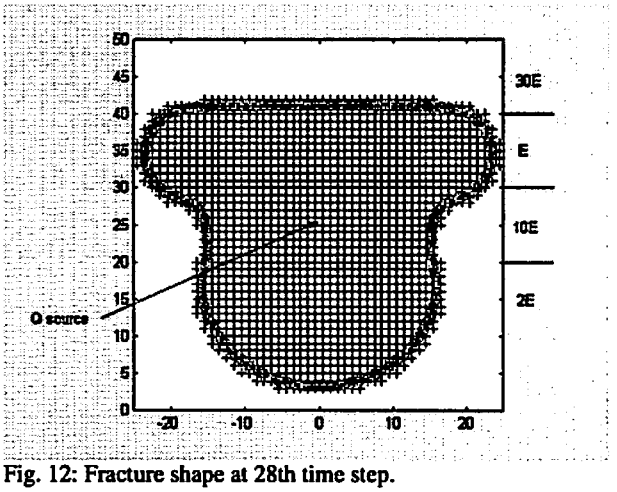

Fig. 12: Fracture shape at 28th time step.

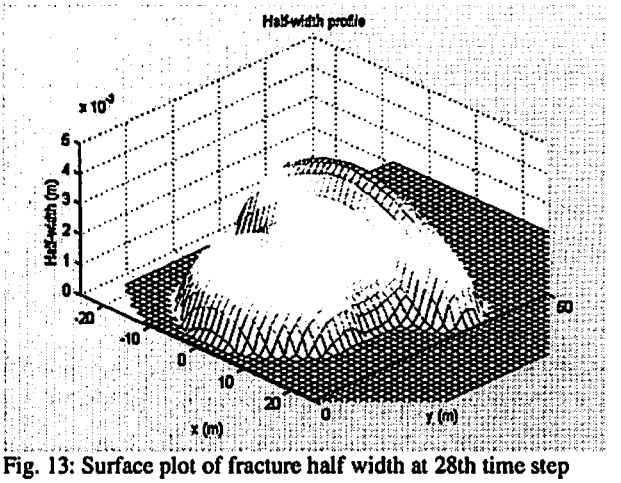

Fig. 13: Surface plot of fracture half width at 28th time step

10 CONCLUSIONS

We have presented a fully coupled method for modeling the propagation of planar 3D hydraulic fractures in laminated reservoirs. The algorithm uses a Fourier-based displacement discontinuity method to generate the layer-dependent influence coefficient matrix. All layers are assumed to be fully bonded together. The fluid flow equations are solved using a standard finite difference scheme. The equations are coupled together using a damped quasi-Newton scheme. The fracture front is advanced, based on the fluid velocities near the fracture tip. The front position is carefully tracked in relation to the parent mesh so as to obtain a smooth front profile despite the use of a binary mesh.

We have demonstrated the accuracy of the scheme, by comparing with available numerical and analytical results. We have also shown that the hydraulic fracture width profile and growth direction is strongly dependent on the elastic properties in each layer. The model serves as a useful tool for the design of hydraulic fractures in laminated reservoirs.

Acknowledgments

The authors thank Schlumberger for permission to publish this work. In addition, the authors wish to thank Steven Crouch, Jean Desroches, Emmanuel Detournay, John Napier, Panos Papanastasiou, and Alexei Savitski for their advice and help in performing benchmark tests with other simulators.

REFERENCES

1) V. M. Narendran and M.P. Cleary, 1983, Analysis of growth and interaction of multiple hydraulic fractures, SPE 12272, presented at Reservoir Simulation Symp., San Francisco, 15-18 Nov 1983.

2) L.N. Germanovich, D.K. Astakhov, M.J. Mayerhofer, J. Shlyapobersky and L.M. Ring, 1997, Hydraulic fracture with multiple segments. I. Observations and model formulation. and II. Modeling., Int. J. Rock Mech. Min. Sci., 34(3/4), paper no 97 and 98.

3) N.R. Warpinski and L. W. Teufel, 1987, Influence of geologic discontinuities on hydraulic fracture propagation, J. of Petroleum Tech., Feb issue, 209-220. and discussion by K.G. Nolte, August 1987, p 998-999.

4) L. W. Taufel and J.A Clark, 1984, Hydraulic fracture propagation in layered rock: experimental studies of fracture containment, paper SPE 9878, SPE J. Feb issue, 19-32.

5) H.R. Warpinski, R.A. Schmidt, and D.A. Northrop, 1982, In-situ stresses: the predominant influence on hydraulic fracture containment. J. of Petroleum Tech., March issue, 653-664.

6) N. Lamont and F.W. Jessen, 1962, The effects of existing fractures in rocks on the extension of hydraulic fractures, SPE 419, 37th annual fall meeting of SPE of AIME, Los Angeles, Oct 7-10 1962.

7) S. Vijayakumar and D.E. Cormack, 1983, Stress behavior in the vicinity of a crack approaching a bimaterial interface, Engrg Fracture Mech., 17(4), 313-321.

8) T.S. Cook and F. Erdogan, 1972, Stresses in bonded materials with a crack perpendicular to the interface, Int. J. Engrg Sci., 10, 677-697.

9) E.R. Simonson, A.S. Abou_Sayed and R.J. Clifton, 1976, Containment of massive hydraulic fractures, SPE 6089, proc: 51st annual fall tech. conf., New Orleans, 3-6 Oct 76.

10) H.A.M. van Eekelen, 1982, Hydraulic fracture geometry: fracture containment in layered formations, SPE 9261, SPE J., June issue, 341-349.

11) M. Thiercelin, 1989, Fracture toughness and hydraulic fracturing, Int. J. Rock Mech. Min. Sci. & Geomech. Abstr. 26(3/4), 177-183.

12) M. Thiercelin, R.G. Jeffrey, and K. Ben Naceur, 1987, The influence of fracture toughness on the geometry of hydraulic fractures. SPE 16431, 441-452.

13) M.A. Biot, W.L. Medlin, L. Masse, 1983, Fracture penetration through an interface, SPE J. Dec issue, 857-869.

14) S.C. Blair, R.K. Thorpe and F.E. Heuze, 1990, Propagation of fluid-driven fractures in jointed rock. Part 2-physical tests on blocks with an interface or lens. Int. J. Rock Mech. Min. Sci. & Geomech. Abstr. 27(4), 255-268.

15) C.E. Renshaw and D.D. Pollard, 1995, An experimentally verified criterion for propagation across unbounded frictional interfaces in brittle, linear elastic material. Int. J. Rock Mech. Min. Sci. & Geomech. Abstr. 32(3), 237-249.

16) A. Peirce and E. Siebrits, 2000, The scaled flexibility matrix method for the efficient solution of boundary value problems in 2D and 3D layered elastic media, accepted by: Computer Meth. in Appl. Mech. & Engrg.

17) A. Peirce and E. Siebrits, 2000, Uniform asymptotic solutions for the accurate solution of cracks intersecting interfaces in layered elastic media, accepted by: Int. J. Fracture.

18) W. Lin and L.M. Keer, 1989, Analysis of a vertical crack in a multilayered medium, J. of Appl. Mech. 56(1), 63-69.

19) S.L. Crouch and A.M. Starfield, 1983, Boundary element methods in solid mechanics, Allen & Unwin, London.

20) A. Savitski and E. Detournay, 1999, Propagation of a penny-shape hydraulic fracture in an impermeable rock, in: Rock Mechanics for Industry (eds: Amadei, Kranz, Scott & Smeallie), Balkema, Rotterdam, 851-858.

21) J.A. Ryder and J.A.L. Napier, 1985, Error analysis and design of a large-scale tabular mining stress analyzer, Proc: Fifth Int. Conf. on Num. Meth. in Geomech., Nagoya, 1549-1555.

22) I.N. Sneddon, 1946, The distribution of stress in the neighbourhood of a crack in an elastic solid, Proc. Roy. Soc. A., 187, 229-260.

23) R.S. Carbonell, 1996, Self-similar solution of a fluid-driven fracture, Ph.D. thesis, Univ. of Minnesota.

24) J.-J. Wang and R.J. Clifton, 1990, Numerical modeling of hydraulic fracturing in layered formations with multiple elastic moduli, in: Rock Mechanics Contributions and Challenges (eds: Hustrulid & Johnson), Balkema, Rotterdam, 303-310.

25) K.-J. Shou and J.A.L. Napier, 1999, A two-dimensional linear variation displacement discontinuity method for three-layered elastic media. Int. J. of Rock Mech. and Min. Sci., 36, 719-729.

26) R.D. Barree, 1983, A practical numerical simulator for three-dimensional fracture propagation in heterogeneous media, SPE paper no. 12273, proc: Reservoir Simulation Symp., San Francisco, 15-18 Nov., 1983, 403-411.

27) W.F. Ames, 1992, Numerical methods for partial differential equations, Academic Press, New York.

28) J. Desroches, E. Detournay, B. Lenoach, P. Papanastasiou, J.R.A. Pearson, M. Thiercelin and A. Cheng, 1994, The crack tip region in hydraulic fracturing, Proc. Roy. Soc. London, Ser. A, 447, 39-48.

APPENDIX A: Discretization of *A* and *B* operator matrices in 1D case

In 1D, the *A* and *B* operators can be discretized as follows. Following the notation of Fig. A.1, the current element, with collocation point *C*, has length $(h_w + h_e)/2$.

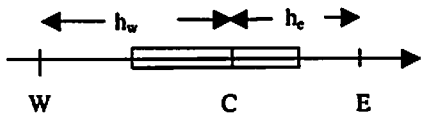

Fig. A.1: 1D coupled model discretization

The neighboring elements have collocation points *W* and *E*. Discretization of $B\delta w$ gives

$$B\delta w = \frac{2}{h_w + h_e}\begin{Bmatrix} D'(w_w)\left(\frac{p_C - p_W}{h_w}\right)\delta w_w - \\ D'(w_e)\left(\frac{p_E - p_C}{h_e}\right)\delta w_e \end{Bmatrix} \qquad (A.1)$$

Noting that

$$\delta w_w = (\delta w_W + \delta w_C)/2 \qquad (A.2)$$

$$\delta w_e = (\delta w_C + \delta w_E)/2 \qquad (A.3)$$

we obtain

$$B\delta w = \frac{1}{h_w + h_e}\begin{Bmatrix} -D'(w_w)\left(\frac{p_C - p_W}{h_w}\right)\delta w_W \\ +D'(w_e)\left(\frac{p_E - p_C}{h_e}\right)\delta w_E \\ +\begin{bmatrix} -D'(w_w)\left(\frac{p_C - p_W}{h_w}\right) \\ +D'(w_e)\left(\frac{p_E - p_C}{h_e}\right) \end{bmatrix}\delta w_C \end{Bmatrix} \qquad (A.4)$$

Similarly the term $A\delta p$ becomes

$$A\delta p = \frac{2}{h_w + h_e}\begin{Bmatrix} \frac{D(w_w)}{h_w}\delta p_W + \frac{D(w_e)}{h_e}\delta p_E \\ -\left[\frac{D(w_w)}{h_w} + \frac{D(w_e)}{h_e}\right]\delta p_C \end{Bmatrix} \qquad (A.5)$$

APPENDIX B: 3D forms for *A* and *B* matrices

In the planar 3D case, the block system of equations has the identical form to the 1D result, except that each component takes on its 3D form. In 3D, the operator matrices *A* and *B* become

$$A = \frac{d}{dx}\left(D(w)\frac{d(\bullet)}{dx}\right) + \frac{d}{dy}\left(D(w)\frac{d(\bullet)}{dy}\right) \qquad (B.1)$$

$$B = \frac{d}{dx}\left(D'(w)\frac{dp}{dx}(\bullet)\right) + \frac{d}{dy}\left(D'(w)\frac{dp}{dy}(\bullet)\right) \qquad (B.2)$$

The planar 3D forms of the discretized *A* and *B* operators can be extrapolated from the 1D formulae, and are given by

$$B\delta w = \frac{1}{h_w + h_e}\begin{Bmatrix} -D'(w_w)\left(\dfrac{p_C - p_W}{h_w}\right)\delta w_W \\ +D'(w_e)\left(\dfrac{p_E - p_C}{h_e}\right)\delta w_E \\ +\left[\begin{matrix} -D'(w_w)\left(\dfrac{p_C - p_W}{h_w}\right) \\ +D'(w_e)\left(\dfrac{p_E - p_C}{h_e}\right)\end{matrix}\right]\delta w_C \end{Bmatrix} +$$

$$\frac{1}{h_s + h_n}\begin{Bmatrix} -D'(w_s)\left(\dfrac{p_C - p_S}{h_s}\right)\delta w_S \\ +D'(w_n)\left(\dfrac{p_N - p_C}{h_n}\right)\delta w_N \\ +\left[\begin{matrix} -D'(w_s)\left(\dfrac{p_C - p_S}{h_s}\right) \\ +D'(w_n)\left(\dfrac{p_N - p_C}{h_n}\right)\end{matrix}\right]\delta w_C \end{Bmatrix} \qquad \text{(B.3)}$$

$$A\delta p = \frac{2}{h_w + h_e}\begin{Bmatrix} \dfrac{D(w_w)}{h_w}\delta p_W + \dfrac{D(w_e)}{h_e}\delta p_E \\ -\left[\dfrac{D(w_w)}{h_w} + \dfrac{D(w_e)}{h_e}\right]\delta p_C \end{Bmatrix} +$$

$$\frac{2}{h_s + h_n}\begin{Bmatrix} \dfrac{D(w_s)}{h_s}\delta p_S + \dfrac{D(w_n)}{h_n}\delta p_N \\ -\left[\dfrac{D(w_s)}{h_s} + \dfrac{D(w_n)}{h_n}\right]\delta p_C \end{Bmatrix} \qquad \text{(B.4)}$$